BROOKHAVEN NATIONAL LABORATORY

BNL-222886-2022-JAAM

Passive oxide film growth observed on the atomic scale

X. Chen, D. Zakharov

To be published in "Advanced Materials Interfaces"

February 2022

Center for Functional Nanomaterials

Brookhaven National Laboratory

U.S. Department of Energy

USDOE Office of Science (SC), Basic Energy Sciences (BES) (SC-22)

Notice: This manuscript has been authored by employees of Brookhaven Science Associates, LLC under Contract No.DE-SC0012704 with the U.S. Department of Energy. The publisher by accepting the manuscript for publication acknowledges that the United States Government retains a non-exclusive, paid-up, irrevocable, world-wide license to publish or reproduce the published form of this manuscript, or allow others to do so, for United States Government purposes.

DISCLAIMER

This report was prepared as an account of work sponsored by an agency of the United States Government. Neither the United States Government nor any agency thereof, nor any of their employees, nor any of their contractors, subcontractors, or their employees, makes any warranty, express or implied, or assumes any legal liability or responsibility for the accuracy, completeness, or any third party's use or the results of such use of any information, apparatus, product, or process disclosed, or represents that its use would not infringe privately owned rights. Reference herein to any specific commercial product, process, or service by trade name, trademark, manufacturer, or otherwise, does not necessarily constitute or imply its endorsement, recommendation, or favoring by the United States Government or any agency thereof or its contractors or subcontractors. The views and opinions of authors expressed herein do not necessarily state or reflect those of the United States Government or any agency thereof.

Passive oxide film growth observed on the atomic scale

*Xiaobo Chen, Zhenyu Liu, Dongxiang Wu, Na Cai, Xianhu Sun, Dmitri N. Zakharov, Sooyeon Hwang, Dong Su, Guofeng Wang, Guangwen Zhou**

X. B. Chen, D. X. Wu, Dr. N. Cai, X. H. Sun, Prof. G. W. Zhou
Materials Science and Engineering Program & Department of Mechanical Engineering, State University of New York at Binghamton, Binghamton, New York 13902, United States
E-mail: gzhou@binghamton.edu

Dr. Z. Y. Liu, Prof. G. F. Wang
Department of Mechanical Engineering and Materials Science, University of Pittsburgh, Pittsburgh, Pennsylvania 15261, United States

Dr. D. N. Zakharov, Dr. S. Hwang, Dr. D. Su
Center for Functional Nanomaterials, Brookhaven National Laboratory, Upton, New York 11973, United States

Keywords: (surface passivation, aluminum, oxidation, *in situ* transmission electron microscopy)

Despite of the ubiquitous presence of passivation on most metal surfaces, the microscopic-level picture of how surface passivation occurs has been hitherto unclear. Using the canonical example of the surface passivation of aluminum, here we employ *in situ* atomistic transmission electron microscopy observations and computational modeling to disentangle entangled microscopic processes and identify the atomic processes leading to the surface passivation. Based on atomic-scale observations of the layer-by-layer expansion of the metal lattice and its subsequent transformation into the amorphous oxide, it is shown that the surface passivation occurs via a two-stage oxidation process, in which the first stage is dominated by intralayer atomic shuffling whereas the second stage is governed by interlayer atomic disordering upon the progressive oxygen uptake. The first stage can be bypassed by increasing surface defects to promote the interlayer atomic migration that results in direct amorphization of multiple atomic layers of the metal lattice. The identified two-stage reaction mechanism and the effect of surface defects in promoting interlayer atomic shuffling can find broader applicability in utilizing surface defects to tune the mass transport and passivation kinetics, as well as the composition, structure and transport properties of the passivation films.

1. Introduction

Nearly all metals spontaneously form a passivating film due to oxidation in their functioning environments. This naturally formed oxide skin governs the real-world interactions of the metal with outer environment and plays a pivotal role in a vast array of technologically important processes ranging from corrosion resistance,[1] catalysis,[2] electrochemistry[3] to fabrication of gate oxides for electronic devices.[4] Therefore, surface passivation has been a topic of intensive interests for both fundamental science and practical technologies.[5] Perhaps the most utilized description of low-temperature passivating film formation is the phenomenological model by Cabrera and Mott, noting that virtually all metals show a similar behavior under ambient conditions.[6] That is, metals display an initial stage of rapid oxide growth, followed by a stage of significantly slower growth to a limiting thickness in the nanometer range.[7] Cabrera-Mott theory stipulates that such self-limiting oxide growth results from a self-generated electric field,[6] where the field-enhanced ionic transport accelerates the initial oxidation but is rapidly attenuated with increasing thickness of the oxide film.[5a, 8] However, the atomic-level and microscopic mechanism underlying such a self-limiting oxide growth behavior has been a longstanding unsettled question since the development of the Cabrera-Mott theory back in 1940s.[6] This is because the formation of a passivating layer requires atomic exchanges between the surface and subsurface regions and directly investigating passivation-induced structure dynamics at the atomic scale has been a major challenge for difficulties in atomically and concurrently resolving the structure evolution in both the surface and subsurface regions. Understanding passivation phenomena has also been complicated by the presence of surface defects and the challenge in directly probing the surface-subsurface interactions at the defective sites.

Directly probing the atomic processes governing the oxygen uptake induced structural transformation of the metallic lattice into a passivating layer of amorphous oxide has not been achieved. This is because the insulating nature of the oxides prohibits the use of many surface-sensitive techniques based on the detection of charged particles such as electrons and ions to both spatially and temporally monitor oxide growth at the buried oxide/metal interfaces and across the entire oxide film. The ultrathin nature of the passivating oxide film also hinders the use of bulk materials science tools to probe the surface and interface regions because of the close proximity. Transmission electron microscopy (TEM) is not subject to such limitations and is capable of providing atomic-scale information for both the surface and subsurface regions at the same time.[9] Particularly, the developments in TEM have allowed temperature-, pressure-, and time-resolved imaging of gas-solid reaction dynamics.[10] By employing a

dedicated environmental TEM equipped with an image corrector and a differential pumping system, here we report an *in situ* study of the surface passivation reaction by flowing O_2 gas in the sample area while simultaneously monitoring the structural dynamics from the outermost surface to deeper atomic layers under the reaction conditions. The *in situ* atomic-scale imaging is complemented by density-functional theory (DFT) calculations and reactive force-field molecular dynamics (ReaxFF MD) simulations. Aluminum (Al) is chosen as a model system because of its wide applications where corrosion-resistance is required (see more details in Figs. S1, S2). We herein uncover the microscopic mechanism of the self-limiting oxide growth and demonstrate that the surface passivation is a two-stage process starting with the intralayer atomic disordering upon the incorporation of oxygen into both the surface and subsurface regions of the metal lattice, followed by interlayer disordering that results in the full amorphization of the oxide layer.

2. Result and Discussion

Fig. 1 presents *in situ* high-resolution TEM (HRTEM) images, in cross-sectional view along the $[1\bar{1}0]$ zone axis, of the Al(111) surface at $pO_2 = 7.3\times10^{-3}$ Pa and 298 K. As shown in Fig. 1(a), the freshly created Al(111) surface is atomically flat and the interplanar spacing matches Al(111) planes. Fig. 1(b) is a HRTEM image of the surface after 2.7 s of O_2 exposure and shows weakened lattice contrast in some areas of the topmost layer (as marked by the dashed white rectangle in Fig. 1(b)). This indicates that the oxygen attack results in the extraction of Al atoms from the topmost Al surface, consistent with the prediction from atomistic simulations.[11] The O adsorption induced extraction of surface atoms becomes more obvious upon the continued O_2 exposure, as shown in Figs. 1(c-e), where the increasingly weakened lattice contrast in the areas marked with the dashed white rectangles indicates the gradual loss of Al atoms from the outermost surface layer. The extraction of Al atoms from the outermost layer opens up channels for the incorporation of O atoms into the subsurface region, resulting in the observed lattice expansion in the areas marked by the dashed cyan rectangles in Figs. 1(d, e). The interplanar spacing of these oxygenated regions undergoes expansion from 0.23 nm of the pristine Al lattice to 0.28 nm. Such O incorporation induced lattice expansion can be termed as paracrystalline (or semicrystalline) disordering,[8, 12] where the intralayer atomic order is lost (as evidenced by the loss of the image contrast of individual atom columns within the individual atomic planes) whereas the interlayer order is still largely maintained (as evidenced by the well resolved interlayer lattice fringes). As seen from the image sequence shown in Figs. 1(d-g), the O incorporation induced paracrystalline disordering propagates both

laterally and vertically, but at a much faster rate along the lateral direction, which results in layer-by-layer oxygenation of the metal lattice planes in the subsurface. The region marked by the dashed line in Fig. 1(f) is the remaining Al lattice that soon transforms into the paracrystalline disorder within ~ 1.5 s (Fig. 1(g)). Upon continued O_2 exposure, the image contrast of interlayer lattice fringes becomes less resolved (Fig. 1(h)) and transforms into an amorphous state within ~ 6 s (Fig. 1(i)). This corresponds to the transition from the initially intralayer disordering to interlayer disordering, thereby resulting in full amorphization of the oxide.

This interlayer disordering also transforms the relatively flat oxide/Al(111) interface to be atomically rough. As marked by the dashed boxes in Figs. 1(d, e), the oxide/Al(111) interface is first observed to exhibit a relatively wide and flat shape, with the presence of atomic ledges during the paracrystalline oxide growth. As the oxidation progresses, the paracrystalline oxide transforms into an amorphous state and the oxide/Al(111) interface becomes atomically rough (Figs. 1(h, i)). The oxide/Al(111) interface maintains the microscopically rough morphology and displays an overall normal movement toward the metal. Figs. 1(j, k) show that the amorphous oxide layer thickens by inward migration of the atomically rough interface, by which arriving O atoms can directly incorporate into the metal lattice at any site of the interface, leading to the continuous oxide growth (such oxide growth with the atomically rough oxide/Al(111) interface is confirmed at multiple places and samples, as shown in supplementary Fig. S3). Detailed tracing of the movement of the oxide/Al(111) interface is depicted in Fig. 1(k), where the relative positions of the interface at 24.9 s and 51 s are given for comparison and show that the interface moves toward the metal by ~ 0.25 nm within an elapsed time of 26.1 s. By contrast, the thickness of the oxide layer increases by ~ 0.32 nm during the same period. Fig. 1(l) shows further measurements of the thickness evolution of the oxide film and the coordinated oxide/interface displacement as a function of time, both of which display an initial rapid increase followed by significantly slower growth to a self-limiting regime. This self-limiting growth behavior can be fitted well with the logarithmic growth law of the Cabrera-Mott model. The difference between the oxide film thickness and the oxide/metal displacement is caused by the oxide formation induced volume expansion (as evidenced by the oxygenation induced lattice expansion in the paracrystalline oxide (Fig. 1(d)) and new oxide formation at both the oxide/Al(111) interface and the outer surface. That is, the oxide film growth is both inward and outward: inward because of the movement of O atoms toward the oxide/metal interface and outward because of the movement of Al atoms toward the oxide surface. The inward and outward oxide growth requires the interlayer atomic shuffling and differs from the

paracrystalline disordering stage that is dominated by intralayer atomic shuffling of Al atoms along with the inward movement of O atoms, as further observed from our ReaxFF MD simulations shown later.

Fig. 2 depicts *in situ* TEM images illustrating the passivation of Al(100). The freshly created (100) surface is atomically flat and oxide-free (Fig. 2(a)). Upon the exposure to $pO_2 = 7.3\times10^{-3}$ Pa at 298 K, the O attack first results in the abstraction of Al atoms from the outermost surface layer, as indicated by the weakened lattice contrast in the regions marked by dashed white rectangles in Figs. 2(b-d). The extraction of Al atoms from the outermost layer facilitates O incorporation into the deeper layers. This results in the intralayer disordering, for which the image contrast of individual atom columns in the oxygenated layers becomes increasingly indistinguishable, as marked by the dashed cyan rectangles in Fig. 2(c-e). This paracrystal disordering propagates laterally and vertically upon the continued O attack, and the interlayer spacing expands from 0.20 nm of the pristine Al lattice to 0.26 nm in the oxygenated region (Fig. 2(e, f)). Upon further O incorporation, the image contrast of interlayer lattice fringes in the oxygenated region becomes increasingly less resolved (Fig. 2(g)) and gradually transforms to the amorphous appearance within ~ 12 s (Fig. 2(h)), indicating the interlayer disordering induced amorphization in the oxide layer.

In contrast to the oxide/Al(111) interface that remains atomically rough during the amorphous oxide growth (Fig. 1), the oxide/Al(100) interface consists of atomically flat (100) terraces and monoatomic ledges (steps). We observe that the oxide growth occurs via lateral flow of ledges along the interface and theses ledges are supplied by repeated nucleation at the oxide/metal interface. As marked by the cyan line in Fig. 2(g), the oxide layer embeds locally into the metal lattice by one atom layer, presumably through an interface O embedment process. This results in the nucleation of two new ledges that subsequently propagate laterally. Fig. 2(g) shows three ledges (numbered 1-3) residing at the oxide/metal interface. Within ~ 12 s of O_2 exposure, step 1 grows out of the field of the TEM view via the ledge flow along the interface (Fig. 2(h)). At the same time, two new interfacial steps (numbered 4, 5 in Fig. 2(h)) are nucleated via the same interfacial O embedment process. All the ledges are observed to sweep laterally, resulting in the coordinated ledge-flow growth of the amorphous oxide along the interface (Figs. 2(h-k)). In the subsequent 21 s, ledges 2 and 3 also grow out of the field of the TEM view (Fig. 2(j)). Fig. 2(k) shows the migration distance of the five ledges over time, illustrating a linear time dependence with a similar ledge velocity of ~ 0.26 nm/s except ledge 3 that has a more defective interface terrace and thus a faster ledge velocity (~ 0.51 nm/s). The more atomic defects in the interface terrace associated with ledge 3 is evident from the much-

weakened image contrast of some atom columns of the metal lattice at the interface (Fig. 2(g)). This indicates that interface terraces are still randomly attacked by arriving O although interface ledges are more favorable for O incorporation, as confirmed from the observed ledge-flow oxide growth. The *in situ* TEM observations show that most of the interfacial ledges have the similar flow velocity, the monatomic ledges propagating in the same direction tend not to merge and form higher steps. Figs. 2(i, j) show that all the terraces maintain atomically flat without nucleating new ledges, indicating that the inward interface migration toward the metal depends on the nucleation frequency of atomic ledges by the O attack to the interface (such oxide growth with the wide and flat oxide/Al(100) interface is confirmed at multiple places and samples, see supplementary Fig. S4). Despite of the absence of nucleating new interface ledges in Figs. 2(i-k), however, the oxide film thickness between the outer surface and the interface terrace as defined by ledges 4 and 5 still increases by ~ 0.35 nm upon the lateral flow of the two existing ledges. This further confirms the interlayer atomic shuffling by the inward movement of O atoms and outward migration of Al atoms, which results in new oxide formation at both the oxide/metal interface and the outer surface, irrespective of crystallographic orientations ((100) vs. (111)). Similar to the (111) oxidation, both the thickness evolution of the oxide film and the oxide/Al(100) interface displacement can be fitted well with the logarithmic growth law of the Cabrera-Mott model, as shown in Fig. 2(l).

The *in situ* TEM observations above show that the passivation of both the Al(111) and (100) surfaces occurs via a two-stage oxidation process. Namely, the first stage is dominated by intralayer disordering whereas the second stage is governed by interlayer disordering that results in the full amorphization of the oxide layer. Fig. 3 illustrates time-sequence HRTEM images demonstrating that the first stage can be largely bypassed by increasing the surface density of atomic defects (mainly atomic steps) to promote the interlayer atomic disordering, where the increased atomic-scale surface roughness is produced *in situ* using a condensed electron beam inside the TEM to bombard clean Al surfaces. Figs. 3(a-d) show the oxidation of a stepped (111) surface. The surface consists of three relatively wide terraces separated by two monatomic steps. Upon the O_2 exposure, the two step regions are first attacked, resulting in the weakened lattice contrast, as indicated by the dashed white circles in Fig. 3(b). This trend becomes more apparent with the continued O_2 exposure. As shown by the yellow circles in Figs. 3(c, d), the step regions are directly transformed into the amorphous oxide whereas the subsurface regions of the terraces as marked with dashed cyan rectangles in Figs. 3(c, d) still adopt the paracrystal feature with the resolved lattice fringes and the expanded lattice spacing of 0.28 nm. Such a difference in the oxide formation between the steps and adjacent flat terraces

illustrates the pronounced effect of surface defects in promoting the interlayer disordering and direct amorphization in the stepped regions.

Figs. 3(e, f) show *in situ* HRTEM images illustrating the passivation of a highly stepped surface with the direct formation of the amorphous oxide upon the O_2 exposure. As marked by the white line in Fig. 3(e), the pristine surface consists of a highly stepped region and less stepped regions with relatively wider (111) terraces. The O_2 exposure results in the direct formation of the amorphous oxide in the highly stepped region but the paracrystalline oxide in the less stepped region, as marked by the dashed white oval and dashed cyan boxes, respectively, in Fig. 3(f). Upon the continued O_2 exposure, the entire surface transforms into a continuous oxide layer and the oxide/metal interface maintains atomically rough during the oxide growth (Figs. 3(g, h). Figs. 3(i-l) show another example illustrating that the further increased density of surface defects can completely suppress the paracrystal disordering. In the beginning, the pristine surface contains a high density of atomic steps with the overall surface orientation along the $[1\bar{1}0]$ direction (Fig. 3(i)). Upon the O_2 exposure, an amorphous oxide thin film develops instantly across the entire surface (Fig. 3(j)). As shown in Figs. 3(j-l), no paracrystal feature of interlayer lattice fringes is visible during the oxide growth, confirming the absence of the intralayer disordering prior to the amorphous oxide formation.

Fig. 4 illustrates that the paracrystalline Al oxide is relatively O-deficient compared to the amorphous Al oxide films. Fig. 4(a) is a scanning TEM (STEM) high-angle annular dark-field (HAADF) image of a corner region at the intersection of two oxidized surface facets. The outer oxide layer has darker contrast because of its relatively lower average atomic mass compared to the Al substrate. Fig. 4(b) is a HRTEM image obtained from the area marked by the dashed white rectangle in Fig. 4(a), showing the amorphous nature of the oxide layer. By contrast, the HRTEM image (Fig. 4(c)) obtained from the intersecting surface as marked with the dashed red rectangle in Fig. 4(a) shows the paracrystalline nature of the oxide layer, as indicated by the presence of interlayer lattice fringes. Such a difference in the oxide growth is related to the nature of the as-prepared pristine surfaces. That is, flat surfaces favor the paracrystal disordering in the first stage of the passivating oxide film growth whereas the rough surfaces result in the direct formation of the amorphous oxide, as has already been shown from the *in situ* TEM image sequences in Figs. 1-3. Fig. 4(d) shows an O elemental map from electron energy loss spectroscopy (EELS) acquired from the region that covers both the amorphous and paracrystalline oxide regions, as marked with the green square in Fig. 4(a). The EELS mapping reveals that the amorphous oxide layer has stronger O intensity than the paracrystalline oxide layer, suggesting that the paracrystalline oxide layer is relatively O-deficient compared to the

amorphous oxide layer. This is further confirmed by spectrum profiles of EELS measurements, showing the stronger peak intensity of the O-K edge from the amorphous oxide layer than that of the paracrystalline oxide layer (Fig. 4(e)). Fig. 4(f) shows EELS Al-K edge spectra from the paracrystalline Al oxide, amorphous Al oxide and the bulk Al, respectively. It can be seen that the EELS Al-K edge spectrum obtained from the paracrystalline oxide resembles more of the metallic Al than the amorphous Al oxide, indicating that Al atoms in the paracrystalline Al oxide film are only partially oxidized because of the deficiency of O. This difference in the oxide composition is further cross-validated by X-ray photoelectron spectroscopy measurements of the surface oxidation of an Al(111) single crystal, showing the increased O/Al atomic ratio of the surface oxide upon the continued O_2 exposure induced paracrystalline → amorphous transformation in the oxide film (supplementary Fig. S5).

The above TEM results and analysis are drawn from various experiments conducted on different regions of various samples. The TEM electron-beam irradiation has a negligible effect on the observed oxide film growth to the limiting thickness of ~2.5 nm after ~ 300 s of the O_2 exposure (more details in SI-5). This is confirmed with "comparison experiments" at multiple surface locations by un-blanking and blanking the electron beam (Figs. S6, S7). In addition, the effect from the possible presence of any background gas molecules (mostly hydrogen, water vapor, carbonyl) in the TEM column is found to be negligible on the observed Al oxide film growth. This is confirmed by *in situ* TEM observations, showing that the Al surfaces maintain oxide-free for a relatively long period of time inside the environmental TEM before flowing O_2 gas in the sample region (Fig. S8).

To further elucidate the microscopic processes underlying the observed paracrystalline and amorphous oxide growth, we performed ReaxFF MD simulations of surface oxidation on flat and stepped Al surfaces. Figs. 5(a-f) show the simulation snapshots illustrating the atomic displacements taken at different O_2 exposure times of the flat Al(100) surface. Figs. 5(c, d) depict the displacement vectors of O and Al atoms between 1 ps and 80 ps, corresponding to the early stage of the oxide film growth. As can be seen, the displacement vectors of O atoms show both components parallel to the oxide surface and toward the metal, indicating the intralayer movement and inward migration towards the Al substrate. By contrast, the displacement vectors for most of the Al atoms are approximately parallel to the oxidized surface, revealing the intralayer shuffling of Al atoms. This simulation duration corresponds to the experimentally observed paracrystal disordering stage (Figs. 1, 2), in which the interlayer lattice planes are still maintained but intralayer atomic order is lost. Fig. 5(b) illustrates a snapshot of the simulation at 200 ps, and Figs. 5(e, f) show the displacement vectors of O and Al atoms

between 101 ps and 200 ps, at the relatively later times of the O_2 exposure. The movements of O atoms still show the intralayer and inward migration components. Meanwhile, we also observe the increased component of the displacement vectors for Al atoms along the direction from the metal towards the oxide surface, indicating the enhanced outward migration of Al atoms. This simulation duration corresponds to the experimentally observed amorphization stage (Figs. 1, 2), in which both the interlayer and intralayer migration of Al atoms take place. The enhanced interlayer mobility of Al atoms can be attributed to the increased O concentration in the oxide film upon the continued O_2 exposure, for which the stronger attractive interactions between O and Al atoms act as the driving force in the interlayer disordering process. This is also corroborated by our experimentally measured higher O content in the amorphous oxide film than that in the paracrystalline oxide (Fig. 4 and Supplemental Fig. S5). Our MD simulations of the oxidation of the stepped surface (Fig. 5(g)) further confirm the effect of higher O content on promoting the interlayer mobility of Al atoms. Figs. 5(h, i) show the MD snapshots taken between 1 ps and 80 ps of the O_2 exposure (same as those in Fig. 5(b, c)). As marked by the dashed magenta circle in Fig. 5(h), the subsurface of the step region shows locally deeper penetration and higher concentration of O atoms than that in the subsurface of the terraces, indicating that surface steps open fast channels for subsurface O incorporation. As a result, the interlayer shuffling of Al atoms is effectively promoted in the vicinity of the step. This is evidenced in Fig. 5(i), where a higher component of the displacement vectors of Al atoms along the vertical direction is observed in the subsurface of the step than that in the subsurface of the terrace. This is consistent with our *in situ* TEM observations (Fig. 3) showing the direct formation of the amorphous oxide in the stepped region by bypassing the paracrystalline oxide formation. It is worth mentioning that the above MD simulation results from the Al(100) surfaces are also valid for both the flat and stepped Al(111) surfaces, which exhibits a similar behavior (Supplementary information Fig. S9).

Furthermore, we discuss our results on the oxide growth at the oxide/metal interfaces. Our *in situ* TEM observations and MD simulations above have shown that the oxide growth involves inward migration of O atoms towards the metal for both the (111) and (100) surfaces, which in turn drives the outward motion of Al atoms. However, a dramatic difference exists for the oxide growth at the oxide/Al(111) and oxide/Al(100) interfaces. That is, the oxide/Al(111) interface is atomically rough and the interface advances towards the metal by random attack of the metal atoms across the interface (Fig. 1). By contrast, the oxide/Al(100) interface is relatively atomically flat and the interface advances through lateral oxide growth by the flow of monatomic interfacial ledges (Fig. 2). To elucidate this difference in the oxide growth between

the two interfaces, DFT calculations were performed to evaluate the adsorption energies for the interfacial incorporation of atomic O into the subsurface of the metal lattice. DFT modeling of the interfaces between an amorphous Al oxide layer and the Al substrate is challenging due to the lack of accurate information about the composition and atomic positions in the amorphous oxide. To avoid such uncertainty in constructing the oxide/metal interfaces, we introduce a monolayer of adsorbed O on the stepped Al(111) and Al(100) surfaces. The DFT structural relaxation results in slightly distorted geometry configurations (Supplementary Fig. S10), which bear a resemblance to a thin layer of Al oxide with the resulting oxide/metal interfaces. We then performed the DFT calculations to compare the adsorption energies for the incorporation of an extra on-surface O atom through the oxide layer into two distinct interstitial sites, one adjacent to the interfacial ledge and the other beneath the interfacial terrace, as marked in Figs. 5(j, k). For the (111) interface, we find that the adsorption energies for the extra O incorporation through the interfacial ledge and terrace are -3.78 eV and -4.21 eV, respectively. Their relatively small difference (0.43 eV) in the adsorption energies suggests the similar reactivity of the interfacial ledge and terrace for O incorporation. Therefore, arriving O atoms can be received across any site of the interface and result in the oxide growth with the atomically rough interface, consistent with our *in situ* TEM observations (Fig. 1). For the (100) interface, by contrast, the adsorption energies for the extra O penetration through the interfacial ledge and terrace are calculated to be -4.79 eV and -3.90 eV, respectively. Their larger difference (0.89 eV) indicates that the interfacial ledge is much more favored for O incorporation than the interfacial terrace. This therefore results in the lateral oxide growth by the ledge mechanism of the interfacial motion, as observed from our *in situ* TEM imaging (Fig. 2).

The Cabrera-Mott theory is commonly cited and employed to explain the passive oxide film growth. However, the microscopic mechanism underlying passive oxide-film formation remains as an outstanding question. A key assumption in the Cabrera-Mott model is that the oxide film grows in a uniform, layer-by-layer fashion. As shown above, our *in situ* HRTEM observations demonstrate that the passivating oxide film occurs via the nucleation and growth of paracrystalline domains induced by the oxygenation of both the surface and subsurface regions of the metallic Al lattice and subsequent transformation of the paracrystalline regions into the amorphous oxide, which represents a critical departure from the uniform, layer-by-layer oxide film growth assumed in the Cabrera-Mott model. This microscopic insight cannot be obtained with the traditional oxidation studies that have been devoted to the kinetics of growing continuous oxide film by measuring the weight gain and oxygen consumption using thermogravimetric analysis without providing structural information. Many recent studies have

employed a wide range of surface science tools to measure the ultrathin amorphous Al oxide film formed from the surface oxidation of Al and its alloys, including composition and chemical state, structural ordering[12b, 13] and the relative stability of amorphous versus crystalline Al oxide films.[7c, 14] However, directly monitoring the microscopic processes of the transformation of a pristine metallic lattice into an amorphous state upon the progressive oxygen uptake has not been achievable. Addressing this issue requires not only resolving the buried oxide/metal interface with the crystal-lattice resolution, but also the capability to capture the structure dynamics of the oxygenated crystal lattice as the surface passivating reaction proceeds. This is not attainable with most surface science tools that are either limited to the topmost layer (such as by scanning tunneling microscopy, low energy electron diffraction) or prone to averaging errors (e.g., XPS or XRD) arising from the temporal and spatial superposition of detected signals originating from several atomic layers of the surface and subsurface region.[7d, 7e, 13a]

The *in situ* atomic-scale TEM observations and analysis bring the detailed insight pivotal to understand the microscopic mechanisms of surface passivation by probing the propagation of the oxygen-uptake induced atomic structural evolution from the surface to deeper atomic layers. Our results show that the oxygenation of the metal lattice induces intralayer disordering with the formation of a paracrystalline oxide that subsequently transforms into an amorphous state by the interlayer disordering driven by increased O uptake. The presence of surface defects provides fast channels for subsurface O incorporation and thus promotes the interlayer disordering for direct amorphization of multiple atomic layers of the metal lattice.

Along with early microscopy and diffraction experiments, evidence has accumulated showing that in systems resistant to corrosion, such as Al,[13b] Ta,[15] Nb,[16] Fe-Cr,[17] Ge,[18] and Si,[4a] native surface films tend to have an amorphous morphology although the microscopic mechanisms of the surface passivation process remain similarly unclear. The effectiveness of the amorphous oxide films as passivating layers is associated with their conformal nature and the lack of defective regions such as grain boundaries and dislocations that exist in polycrystalline films which would enhance the transport of metal and oxygen ions.[16, 19] The atomistic mechanisms of Al oxide film growth observed here provide insight into the microscopic processes underlying the surface passivation reactions. Particularly, the identified two-stage reaction mechanism and the effect of surface defects in promoting interlayer atomic shuffling can find broader applicability in utilizing surface defects to tune the passivation kinetics and the composition, atomic structure and transport properties of the resultant passivation films.

3. Conclusion

In summary, we have used *operando* electron microscopy to atomically monitor the dynamic process governing the surface passivation of Al. Our *in situ* observations demonstrate that the surface passivation occurs via a two-stage process starting with the intralayer atomic disordering upon the incorporation of oxygen into both the surface and subsurface region of the metal lattice, followed by interlayer disordering that leads to full amorphization of the oxide layer. The presence of surface defects can promote the interlayer disordering for direct amorphization of multiple atomic layers of the metal lattice. The identified two-stage reaction mechanism and the effect of surface defects in promoting interlayer atomic shuffling can find broader applicability in utilizing surface defects to tune the composition, structure and transport properties of the passivation films.

4. Experimental and Computational Section

Al thin foils with an average normal thickness of ~ 50 nm were prepared using a combination of Focused Ion Beam (FIB) lift-out techniques and low-energy milling. To minimize potential structure damage and Ga contamination, a lower voltage (5 kV) and current (9 pA) of the Ga ion beam was used to trim the surface of the sliced sample in the final stage of the FIB process. The Al slice was loaded on a Mo Omniprobe Lift-out grid and further polished by a NanoMill TEM specimen preparation system with a low voltage (900 V) and current (80 pA) of Ar^+ ions to remove surface damage and contamination. The as-prepared Al thin foils were then examined by HRTEM imaging and EDS analyses, confirming that the structure damage and contamination from the FIB process is negligible (Fig. S1). *In situ* TEM experiments were performed using a dedicated differential pumping environmental TEM (FEI Titan 80-300) equipped with an image aberration corrector. The microscope has a spatial resolution of 0.8 Å in the high-resolution TEM mode. Atomically clean Al surfaces were obtained using a condensed electron beam inside the TEM to sputter off the air-formed native oxide (Fig. S2) and generate holes with well-defined facets.[12a] These freshly generated facets are oxide-free and ideal for *in situ* TEM observations of surface passivation from the beginning. Complete removal of the native oxide and surface cleanliness were confirmed by HRTEM

imaging, electron diffraction and electron energy loss spectroscopy. High-purity O_2 (~ 99.9999%) was introduced into the sample area through a leak valve to oxidize the Al foils at a given temperature and pressure. *In situ* TEM observations of the oxidation process were made in the cross-section views, by imaging along Al edges of empty holes created *in situ*. EEL spectra of the O K-edge were acquired from the intersection region of two oxidized Al facets using Talos (FEI F200X) equipped with a Gatan EELS detector. The spectra were obtained in the HAADF-STEM mode. Spectra were aligned with reference to the zero-loss peak position.

We performed MD simulations of Al oxidation using the LAMMPS code[20] to corroborate the *in situ* TEM observations. The bonding between Al and O atoms was described using the Reactive Force-Field Method (ReaxFF),[21] in which force field parameters were developed by Hong and Van Duin.[22] All MD calculations were carried out at a constant temperature of T= 298 K in the canonical (NVT) ensemble employing a Nosé–Hoover thermostat.[23] The equation of motion was integrated using a timestep of 0.1 fs to accurately capture the adsorption, dissociation and diffusion of O_2 molecules on aluminum surface as suggested by Hong and Van Duin.[23] The scheme of simulation box applied in this study was similar with that previously used by Hasnaoui et al.[24] The Al(100) and (111) surfaces were represented by slab models with the approximate dimensions of $4.05\times4.05\times3.07$ nm^3 and $4.05\times4.01\times2.60$ nm^3, respectively. The vacuum volume was added to the top of each slab, and periodic boundary condition was imposed in all three dimensions. O_2 molecules, with the density of 0.2 gram/cm^3, were randomly distributed in the vacuum volume. To avoid the unphysical overlapping of O_2 molecules, the interatomic distance of O atoms in two separate molecules was kept greater than three times of the O-O bond length. The MD simulations were performed with a maximum simulation time of 0.1 ns to investigate the initial oxidation mechanism of Al(100) and (111) surfaces under oxidation conditions. In addition, individual surface atomic steps were introduced to the slab model in order to compare the dynamic oxidation behaviors with or without surface defects.

Density-functional theory (DFT) calculations were performed using the Vienna ab-initio simulation package (VASP)[25] with the Perdew-Burke-Ernzerhof (PBE) generalized gradient approximation (GGA) and projector augmented wave (PAW) potentials.[26] Previous studies have confirmed that a cutoff energy of 400 eV is sufficient for well converged system energy. Interfacial steps were modeled using k-point sampling based on the (4×4×1) Monkhorst-Pack mesh.[25–27] Interfacial O incorporation was modeled with stepped Al(100) and (111) surfaces covered by a monolayer of adsorbed O. Stepped Al surfaces were constructed by cleaving supercells made from bulk Al. Successive slabs with five atomic layers were separated by a vacuum region of 12 Å. The positions of the atoms in the two bottom layers were fixed, while the positions of the atoms in the top three layers were allowed to relax until all force components on each of them were less than 0.02 eV/Å. The lattice parameters of Al were calculated to be 4.04 Å, which is in good agreement with previous calculations[28] and the experimental values of 4.05 Å.[29]

We investigated the O adsorption energies and structure evolution by sequentially adsorbing a single O atom for each calculation. The O adsorption energy E_{ads} was calculated as

$$E_{ads}=E_{O/Al}^{tot}-E_0-\frac{No}{2}E_{O_2}, \qquad (1)$$

where $E_{O/Al}^{tot}$ and E_0 are the total energy of the whole Al-O system and the energy of the most stable configuration with one fewer adsorbed O atom compared with the system, respectively. E_{O_2} is energy of an isolated O_2 molecule, and No is number of the adsorbed O. The atomic structures are visualized using the Visualization for Electronic and Structure Analysis (VESTA).

Supporting Information

Supporting Information is available from the Wiley Online Library or from the author.

Acknowledgements

This work was supported by the U.S. Department of Energy (DOE), Office of Basic Energy Sciences, Division of Materials Sciences and Engineering under Award No. DE-SC0001135. This research used resources of the Center for Functional Nanomaterials and the Scientific Data and Computing Center, a component of the Computational Science Initiative, which is a U.S. DOE Office of Science Facility, at Brookhaven National Laboratory under Contract No. DE-SC0012704. G. Wang gratefully acknowledge the financial support from the National Science Foundation under DMR 1905572/1905422 for the computational work. This research also used the computational resources provided by the University of Pittsburgh Center for Research Computing and the Extreme Science and Engineering Discovery Environment (XSEDE) supported by National Science Foundation grant number OCI-1053575.

Conflict of Interest

The authors declare no conflict of interest.

Received: ((will be filled in by the editorial staff))
Revised: ((will be filled in by the editorial staff))
Published online: ((will be filled in by the editorial staff))

References

[1] a) X. G. Li, D. W. Zhang, Z. Y. Liu, C. W. Du, C. F. Dong, *Nature* **2015**, *527*, 441; b) P. Marcus, *Corrosion mechanisms in theory and practice*, CRC press, **2011**; c) X. X. Yu, A. Gulec, Q. Sherman, K. L. Cwalina, J. R. Scully, J. H. Perepezko, P. W. Voorhees, L. D. Marks, *Phys. Rev. Lett.* **2018**, *121*, 145701.

[2] S. Shaikhutdinov, H. J. Freund, *Annu. Rev. Phys.* Chem. **2012**, *63*, 619.

[3] a) A. Sarkar, Q. S. Wang, A. Schiele, M. R. Chellali, S. S. Bhattacharya, D. Wang, T. Brezesinski, H. Hahn, L. Velasco, B. Breitung, *Adv. Mater.* **2019**, *31*, 1806236; b) X. G. Zhang, *Electrochemistry of Silicon and its Oxide*, Springer Science & Business Media, **2007**.

[4] a) D. A. Muller, T. Sorsch, S. Moccio, F. H. Baumann, K. Evans-Lutterodt, G. Timp, *Nature* **1999**, *399*, 758; b) K. Nomura, H. Ohta, A. Takagi, T. Kamiya, M. Hirano, H. Hosono, *Nature* **2004**, *432*, 488.

[5] a) J. D. Baran, H. Grönbeck, A. Hellman, *Phys. Rev. Lett.* **2014**, *112*, 1; b) K. Leistner, C. Toulemonde, B. Diawara, A. Seyeux, P. Marcus, *J. Electrochem. Soc.* **2013**, *160*, C197.

[6] N. Cabrera, N.F. Mott, *Reports Prog. Phys.* **1949**, *12*, 163.

[7] a) F. Reichel, L. P. H. Jeurgens, E. J. Mittemeijer, *Acta Mater.* **2008**, *56*, 2897; b) Q. Q. Liu, X. Tong, G. W. Zhou, *Langmuir* **2015**, *31*, 13117; c) L. P. H. Jeurgens, W. G. Sloof, F. D. Tichelaar, E. J. Mittemeijer, *Phys. Rev. B* **2000**, *62*, 4707; d) N. Cai, G. W. Zhou, K. Müller, D. E. Starr, *Appl. Phys. Lett.* **2012**, *101*, 1; e) N. Cai, G. W. Zhou, K. Müller, D. E. Starr, *Phys. Rev. B - Condens. Matter Mater. Phys.* **2011**, *84*, 1; f) N. Cai, Q. Q. Liu, X. Tong, G. W. Zhou, *Langmuir* **2014**, *20*, 774; g) N. Cai, H. L. Qin, T. Xiao, G. W. Zhou, *surf. sci.* **2013**, *618*, 20; h) N. Cai, G. W. Zhou, K. Muller, D. E. Starr, *J. Phys. Chem. C* **2013**, *117*, 172.

[8] N. Cai, G. W. Zhou, K. Müller, D. E. Starr, *Phys. Rev. Lett.* **2011**, *107*, 35502.

[9] a) A. M. Thron, J. Gao, B. Ercan, M. A. Laurent, S. Chowdhury, K. V. Benthem, *Phys. Status Solidi.* **2021**, *218*, 2100304; b) Y. Zhai, Y. Chen, Y. Zhao, H. Long, X. Li, Q. Deng, H. Lu, X. Yang, G. Yang, W. Li, L. Yang, S. Mao, Z. Zhang, A. Li, X. Han, *Acta Mater.* **2021**, *215*, 116991; c) Q. Jeangros, T. W. Hansen, J. B. Wagner, R. E. Dunin-Borkowski, C. Hébert, A. Hessler-Wyser, *Acta Mater.* **2014**, *67*, 362; d) X. H. Sun, W. H. Zhu, D. X. Wu, C. R. Li, J. Y. Wang, Y. G. Zhu, X. B. Chen, J. A. Boscoboinik, R. Sharma, G. W. Zhou, *Nat. Commun.* **2020**, *11*, 305; e) T. L. Barth, E. A. Marquis, *Oxid. Met.* **2021**, *95*, 293; f) M. Song, G. Zhou, N. Lu, J. Lee, E. Nakouzi, H. Wang, D. S. Li, *Science* **2020**, *367*, 40; g) X. B. Chen, D. X. Wu, L. F. Zou, Q. Y. Yin, H. L. Zhang, D. N. Zakharov, E. A. Stach, G. W. Zhou, *Chem. Commun.* **2018**, *54*, 7342; h) L. F. Zou, J. Li, D. Zakharov, E. A. Stach, G. W. Zhou, *Nat. Commun.* **2017**, *8*, 307; i) G. W. Zhou, L. L. Luo, L. Li, J. Ciston, E. A. Stach, W. A. Saidi, J. C. Yang, *Chem. Commun.* **2013**, *49*, 10862.

[10] a) C. S. Bonifacio, G. Das, I. M. Kennedy, K. V. Benthem, *J. Appl. Phys.* **2017**, *122*, 234304; b) X. Yang, Z. An, Y. Zhai, X. Wang, Y. Chen, S. Mao, X. Han, *Corros. Sci.* **2021**, *191*, 109711; c) Q. Jeangros, T. W. Hansen, J. B. Wagner, C. D. Damsgaard, R. E. Dunin-Borkowski, C. Hebert, A. Hessler-Wyser, *J. Mater. Sci.* **2013**, *48*, 2893; d) T. Uchiyama, H. Yoshida, Y. Kuwauchi, S. Ichikawa, S. Shimada, M. Haruta, S. Takeda, *Angew. Chemie - Int. Ed.* **2011**, *50*, 10157; e) M. Togaru, R. Sainju, L. Zhang, W. Jiang, Y. Zhu, *Mater. Charact.* **2021**, *174*, 111016; f) L. Sun, K. W. Noh, J. G. Wen, S. J. Dillon, *Langmuir* **2011**, *27*, 14201; g) L. Li, L. L. Luo, J. Ciston, W. A. Saidi, E. A. Stach, J. C. Yang, G. W. Zhou, *Phys. Rev. Lett.* **2014**, *113*, 136104; h) G.W. Zhou, L. L. Luo, L. Li, J. Ciston, E. Stach, J. C. Yang, *Phys. Rev. Lett.* **2012**, *109*, 235502; i) L. L. Luo, L. Li, D. K. Schreiber, Y. He, D. R. Baer, S. M. Bruemmer, C. M. Wang, *Sci. adv.* **2020**, *6*, eaay8491.

[11] a) H. Brune, J. Wintterlin, J. Trost, G. Ertl, J. Wiechers, R. J. Behm, *J. Chem. Phys.*

1993, *99*, 2128; b) C. Lanthony, J. M. Ducéré, M. D. Rouhani, A. Hemeryck, A. Estève, C. Rossi, *J. Chem. Phys.* **2012**, *137*, 094707; c) D. E. Oner, H. Ternow, R. Chakarova, B. Kasemo, I. Zorić, *Surf. Sci.* **2002**, *512*, L325.

[12] a) L. Nguyen, T. Hashimoto, D. N. Zakharov. E. A. Stach, A. P. Rooney, B. Berkels, G. E. Thompson, S. J. Haigh, T. L. Burnett, *ACS Appl. Mater. Interfaces.* **2018**, *10*, 2230; b) P. C. Snijders, L. P. H. Jeurgens, W. G. Sloof, *Surf. Sci.* **2005**, *589*, 98.

[13] a) L. P. H. Jeurgens, W. G. Sloof, F. D. Tichelaar, E. J. Mittemeijer, *Thin Solid Films* **2002**, *418*, 89; b) F. Reichel, L. P. H. Jeurgens, G. Richter, P. A. V. Aken, E. J. Mittemeijer, *Acta Mater.* **2007**, *55*, 6027.

[14] F. Reichel, L. P. H. Jeurgens, E. J. Mittemeijer, *Phys. Rev. B* **2006**, *74*, 144103.

[15] B. Shyam, K.H. Stone, R. Bassiri, M.M. Fejer, M.F. Toney, A. Mehta, *Sci. Rep.* **2016**, *6*, 1.

[16] P. N. Rojas, S. E. Rodil, *Int. J. Electrochem. Sci.* **2012**, *7*, 1443.

[17] V. Maurice, W. P. Yang, P. Marcus, *J. Electrochem. Soc.* **2019**, *143*, 1182.

[18] T. Hanrath, B. A. Korgel, *J. Am. Chem. Soc.* **2004**, *126*, 15466.

[19] Y. Yang, A. Kushima, W. Z. Han, H. L. Xin, J. Li, *Nano Lett.* **2018**, *18*, 2492.

[20] S. Plimpton, *J. Comput. Phys.* **1995**, *117*, 1.

[21] A. C. T. Van Duin, S. Dasgupta, F. Lorant, W. A. Goddard, *J. Phys. Chem. A* **2001**, *105*, 9396.

[22] S. Hong, A. C. T. Van Duin, *J. Phys. Chem. C* **2016**, *120*, 9464.

[23] S. Nosé, *J. Chem. Phys.* **1984**, *81*, 511.

[24] A. Hasnaoui, O. Politano, J. M. Salazar, G. Aral, R. K. Kalia, A. Nakano, P. Vashishta, *Surf. Sci.* **2005**, *579*, 47.

[25] G. Kresse, J. Hafner, Phys. Rev. B **1994**, *49*, 14251.

[26] G. Kresse, J. Furthmüller, *Comput. Mater. Sci.* **1996**, *6*, 15.

[27] P.E. Blöchl, *Phys. Rev. B* **1994**, *50*, 17953.

[28] K. Honkala, K. Laasonen, *Phys. Rev. Lett.* **2000**, *84*, 705.

[29] A. L. Ortiz, L. Shaw, *Acta Mater.* **2004**, *52*, 2185.

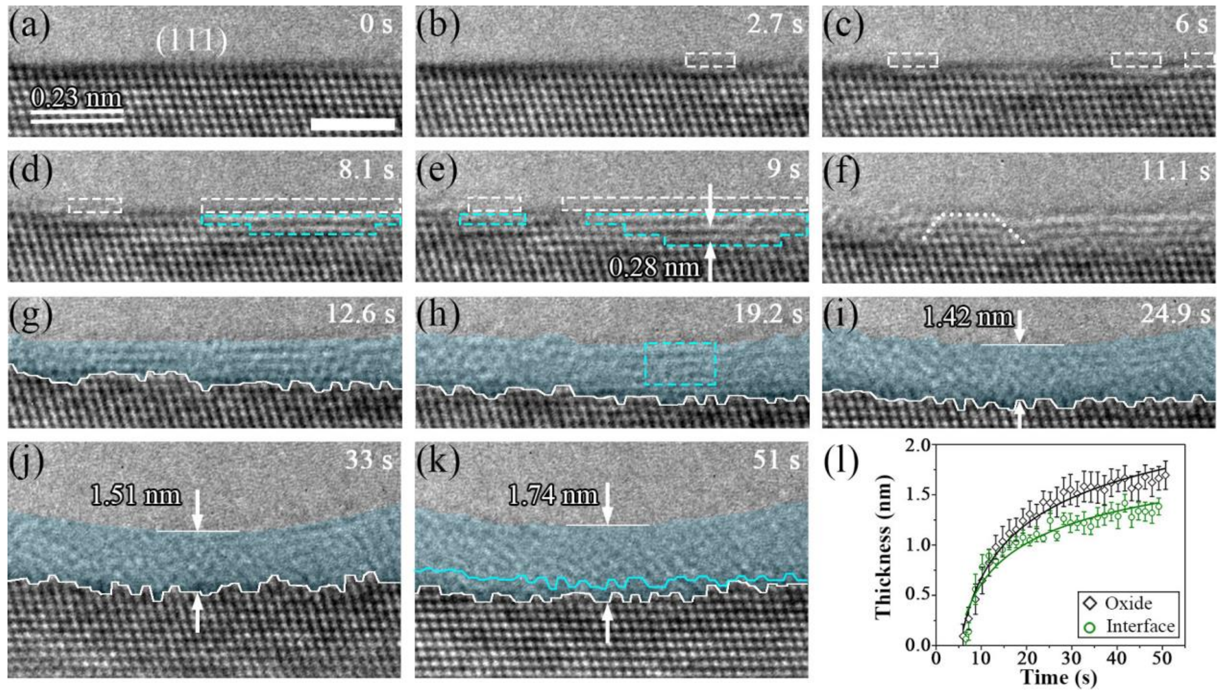

Figure 1. Passive oxide film formation on Al(111). (a-l) Time-sequence HRTEM images (Supplementary Movie 1) showing O adsorption induced extraction of Al atoms from the outermost surface of pristine Al(111), followed by the layer-by-layer oxidation of the metal lattice planes in the subsurface into a paracrystalline oxide layer that gradually transforms into an amorphous Al oxide layer upon the continued O_2 exposure at 298 K in $pO_2 \approx 7.3\times10^{-3}$ Pa. The dashed white and cyan rectangles mark the extracted topmost layer and the paracrystalline oxide regions, respectively. The solid white lines mark the oxide/metal interface. The pseudo color is applied to the oxide layer to guide the eye. The solid cyan line in (l) is the superimposed trace of the position and profile of the oxide/metal interface at t=24.9 s in (i), showing the inward movement of the interface toward the metal. Scale bar, 2 nm.

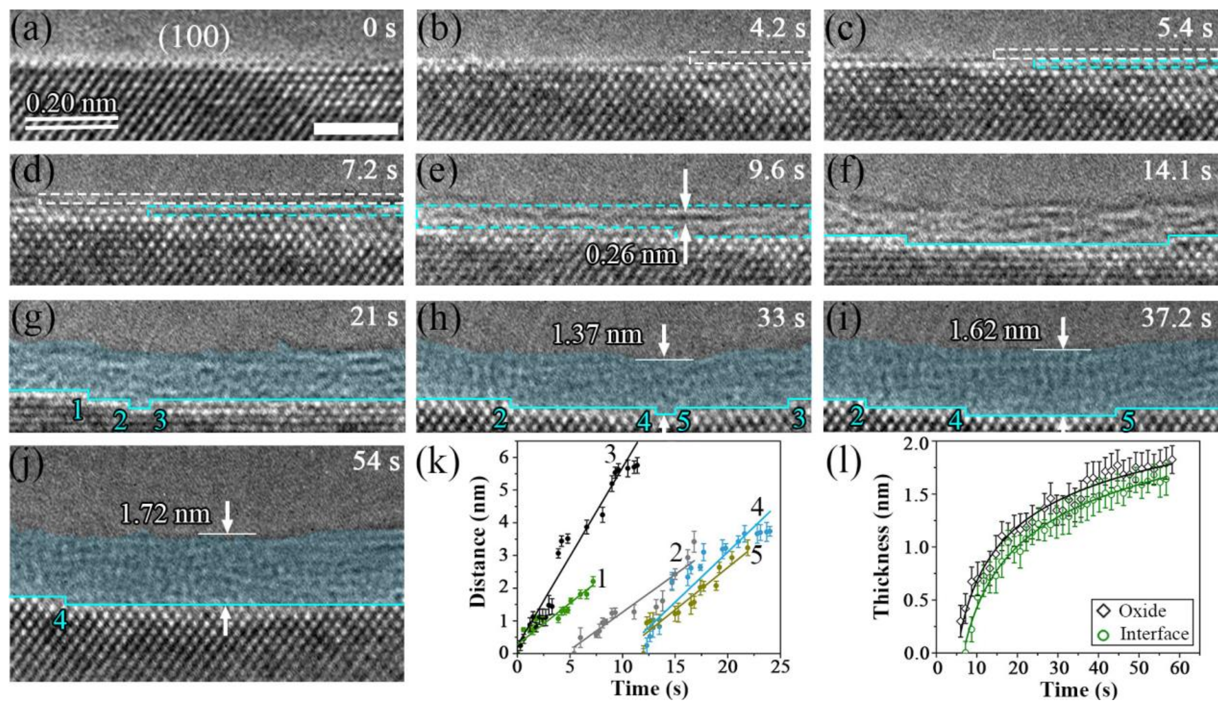

Figure 2. Passive oxide film formation on Al(100). (a-k) Time-elapse sequence of HRTEM images (Supplementary Movie 2) showing the two-stage oxide-film formation on Al(100) at 298 K in $pO_2 \approx 7.3\times10^{-3}$ Pa. The dashed white rectangles correspond to the weakened lattice contrast regions upon the O adsorption induced abstraction of Al atoms from the topmost surface region. The dashed cyan rectangles mark the paracrystal oxide regions. The cyan lines mark the oxide/metal interface and lateral flow of interfacial ledges 1-5. Scale bar, 2 nm. The pseudo color is applied to the oxide layer to guide the eye. (l) Measured ledge positions versus time for five independent monoatomic interfacial ledges, the error bars represent standard deviation uncertainties based on multiple measurements at different interfacial locations. The solid lines correspond to a linear fit to the experimental data points.

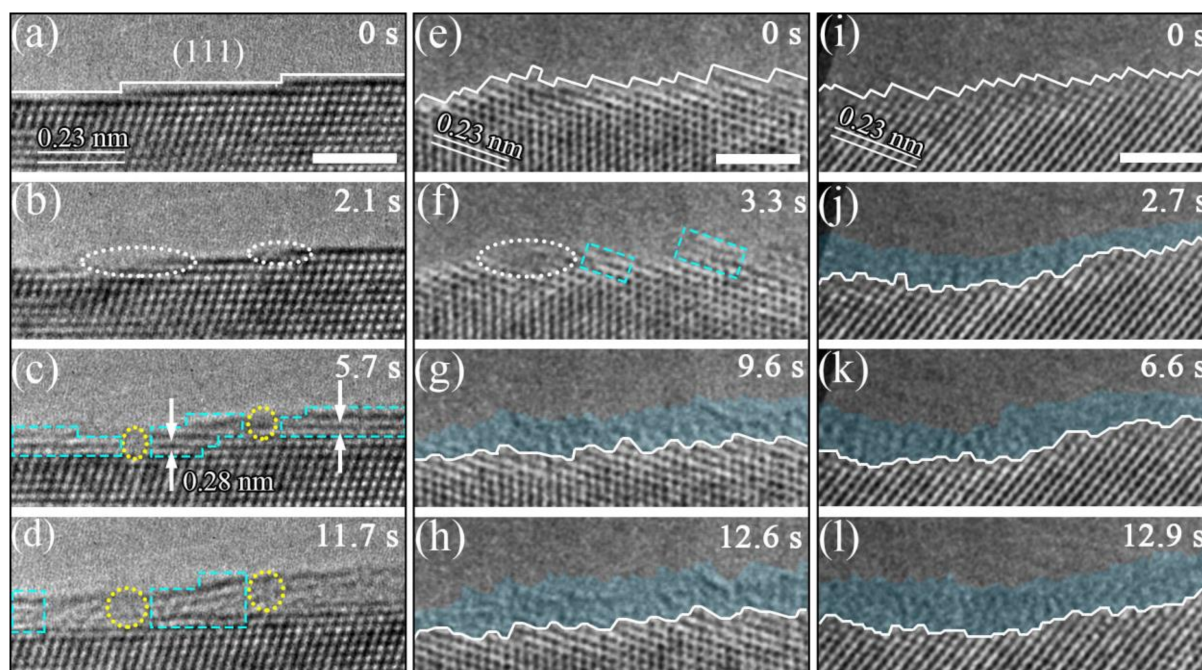

Figure 3. Promoting passive oxide film formation by surface defects. (a-d) Time-sequence HRTEM images (Supplementary Movie 3) showing the oxidation of an Al(111) surface consisting of terraces and well-separated monatomic steps. Dashed white ovals mark the preferential oxidation at the surface steps. Dashed yellow circles and cyan rectangles mark the direct formation of amorphous Al oxide at the step edges and paracrystal Al oxide at the terraces, respectively. (e-h) Time-sequence HRTEM images (Supplementary Movie 4) showing the oxidation of an Al surface consisting of highly stepped regions and relatively wide terraces. The dashed white oval marks the direct formation of amorphous Al oxide in the highly stepped region. Dashed cyan rectangles outline the formation of the paracrytal oxide that subsequently transforms into the amorphous Al oxide in the terrace regions. (i-l) Time-sequence HRTEM images (Supplementary Movie 5) showing the oxidation of a highly stepped Al surface. The O_2 exposure results in the direct formation of an amorphous Al oxide film across the entire surface. All the *in situ* TEM images were captured at 298 K and $pO_2 \approx 7.3\times10^{-3}$ Pa of O_2 gas flow. Scale bar, 2 nm. The pseudo color is applied to the oxide layer to guide the eye.

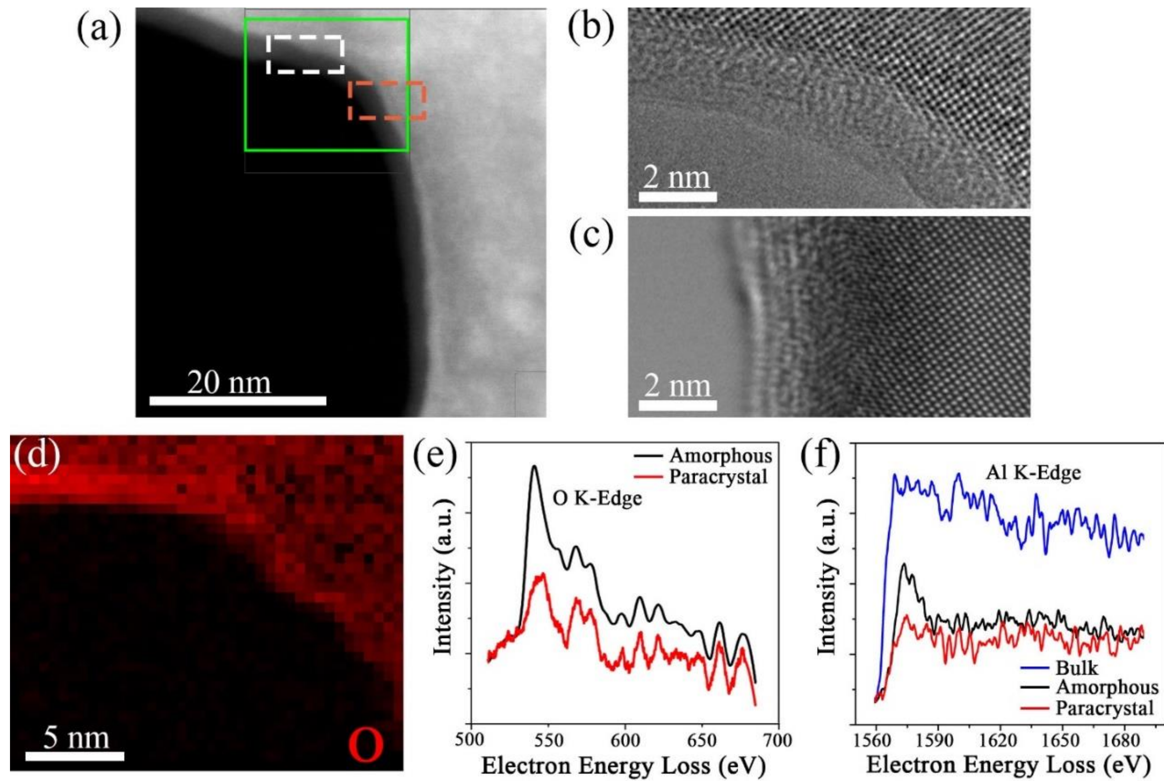

Figure 4. Composition analysis of the paracrystalline and amorphous Al oxide films. (a) HAADF-STEM image of an intersection region of two oxidized facets. (b) HRTEM image obtained from the surface marked by the dashed white rectangle in (a), showing the presence of an amorphous Al oxide layer. (c) HRTEM image obtained from the adjacent surface marked by the dashed red rectangle in (a), showing the presence of a paracrystalline Al oxide layer. (d) STEM EELS O map of the corner region marked by the green rectangle in (a). (e) STEM EELS O K-edge spectra obtained from the amorphous (black) and paracrystalline (red) Al oxide films, respectively. (f) STEM EELS Al K-edge spectra obtained from the amorphous Al oxide, paracrystalline Al oxide, and the bulk Al, respectively.

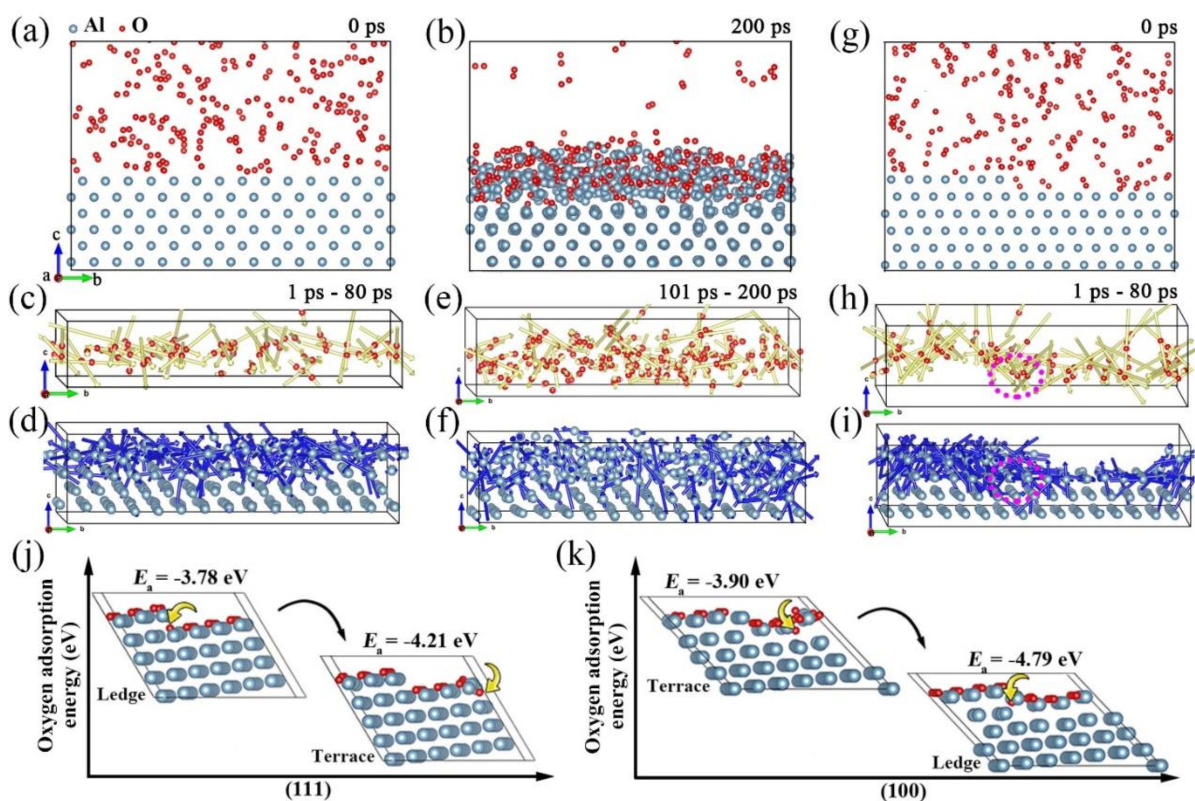

Figure 5. ReaxFF MD and DFT simulations of oxidation of Al surfaces. (a, b) Snapshots of MD simulations of the oxidation of a flat Al(100) surface at 0 ps and 200 ps of O_2 exposure (Supplementary Movies 6, 7). (c, d) Displacement vectors of O and Al atoms between 1 ps and 80 ps of O_2 exposure. (e, f) Displacement vectors of O and Al atoms between 101 ps and 200 ps of O_2 exposure. (g-i) MD simulations of the oxidation of a stepped Al(111) surface and displacement vectors of O and Al atoms between 1 ps and 80 ps of O_2 exposure (Supplementary Movie 8). The dashed magenta circles in (h, i) mark the stepped region, showing the locally promoted interlayer displacement of O and Al atoms. (j, k) DFT calculations of O incorporation into distinct subsurface sites of stepped Al(111) and Al(100) surfaces with a monolayer of pre-adsorbed O. For the (111) interface, the subsurface of the interfacial terrace is slightly more favorable than that of the interfacial ledge for O incorporation. By contrast, the subsurface site of the interface ledge is pronouncedly more favorable than that of the interfacial terrace for O incorporation by the Al(100) surface. The blue and red balls stand for Al and O atoms, respectively.

Supporting Information

Passive oxide film growth observed on the atomic scale

*Xiaobo Chen, Zhenyu Liu, Dongxiang Wu, Na Cai, Xianhu Sun, Dmitri N. Zakharov, Sooyeon Hwang, Dong Su, Guofeng Wang, Guangwen Zhou**

This file includes:

Supplementary text (SI 1-8)

Figures S1 to S10

Legends for Movies S1 to S13

SI References

Other supplementary materials for this manuscript include the following:

Movies S1 to S13

SI-1. TEM EDS analysis of the as-prepared Al thin foil specimens

The Al thin foils prepared with a combination of FIB and NanoMilling were examined by energy-dispersive X-ray spectroscopy (EDS). The EDS analysis was performed with Talos (FEI F200X) equipped with a four-quadrant EDS detector. Fig. S1 shows a representative EDS spectrum, in which the Mo and Cu signals are from the Mo Omniporbe grid and the Cu spacer, respectively, the weak O signal from the native Al oxide. The absence of the signal in the Ga region confirms negligible Ga contamination from the FIB process.

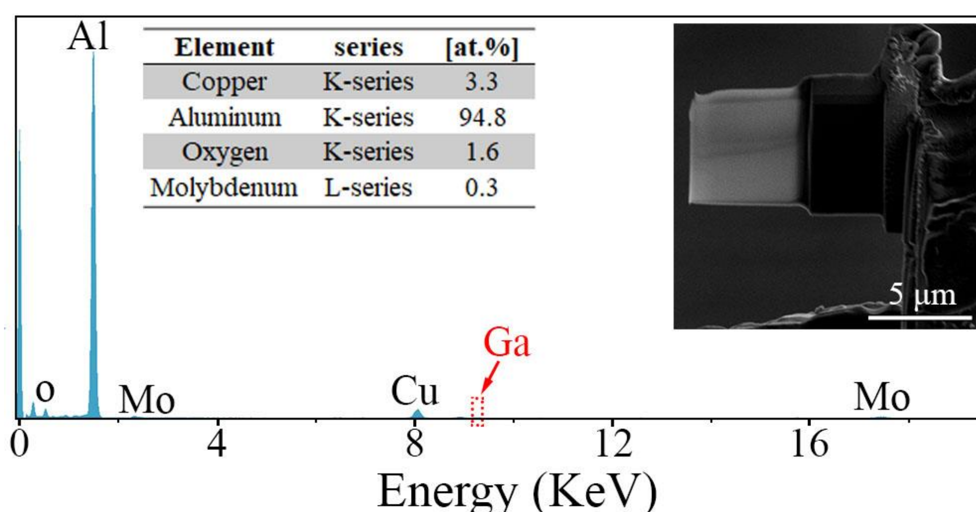

Element	series	[at.%]
Copper	K-series	3.3
Aluminum	K-series	94.8
Oxygen	K-series	1.6
Molybdenum	L-series	0.3

Figure S1: EDS collected from an Al thin foil specimen prepared by a combination of FIB and NanoMilling. The Mo and Cu signals are from the Mo Omniporbe grid and the Cu spacer, respectively, the weak O signal from the native Al oxide. The absence of the intensity in the Ga region (marked in red) indicates negligible Ga contamination from the FIB process. The insets are an SEM image of the Al thin foil specimen, and the composition quantification of the elements present in the EDS spectrum.

SI-2. Characterization of the air-formed native Al oxide

The native air-formed Al oxide on the as-prepared Al thin foils was characterized by HRTEM and EELS. Fig. S2(a) illustrates a HRTEM image, showing an amorphous nature of the Al native oxide with a thickness of ~ 4.3 nm, which is thicker than the limiting thickness of the oxide film (~ 2.5 nm) formed from the *in situ* oxidation at the low O_2 gas pressure inside the ETEM. Fig. S2(b) shows the STEM EELS O K-edge mapping. Fig. S2(c) shows the corresponding EELS line-scan acquired along the direction from the vacuum region toward the oxide layer and the Al substrate of the same region, as marked with the white arrow in Fig. S2(b). This native oxide layer can be sputtered off inside the TEM with the use of a condensed electron beam, thereby resulting in a freshly cleaned Al surface for *in situ* oxidation.

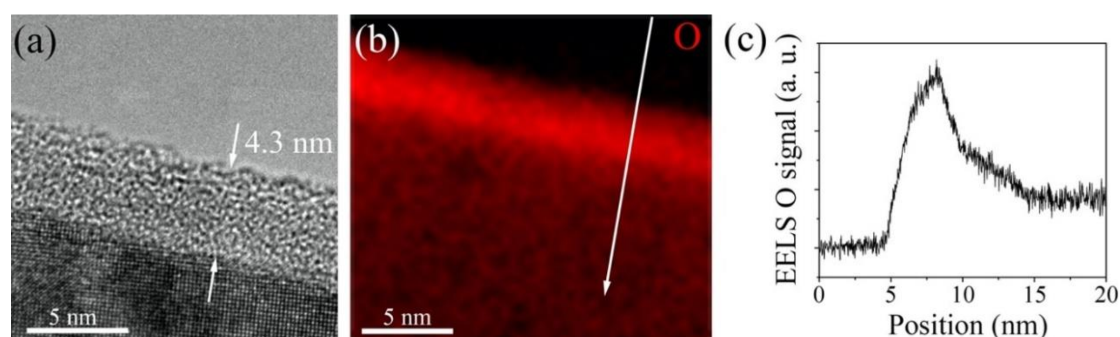

Figure S2. Characterizations of the native air-formed oxide on an as-prepared Al thin foil. (a) HRTEM image illustrating the amorphous nature of the native Al oxide layer formed in the ambient air. (b) STEM EELS O mapping. (c) Corresponding EELS line-scan of the same region along the direction marked with the white arrow in (b).

SI-3. *In situ* TEM observations performed on various Al samples

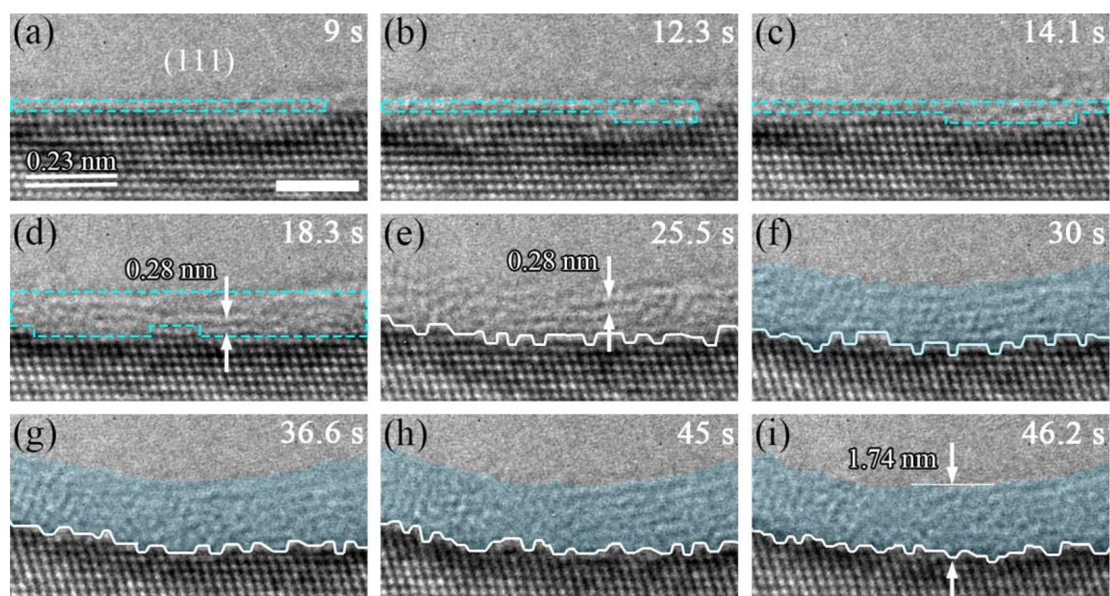

Figure S3: Passive oxide film formation on Al(111) (a-i) Time-sequence HRTEM images (Supplementary Movie 9) showing the two-stage oxide film formation. The oxygenation first results in the layer-by-layer formation of the paracrystalline oxide that gradually transforms into an amorphous Al oxide layer upon the continued O_2 exposure at T=298 K in $pO_2 \approx 9.3\times10^{-3}$ Pa. The dashed cyan rectangles mark the paracrystalline oxide regions. The solid white lines mark the oxide/metal interface. Scale bar, 2 nm. The pseudo color is applied to the oxide layer to guide the eye.

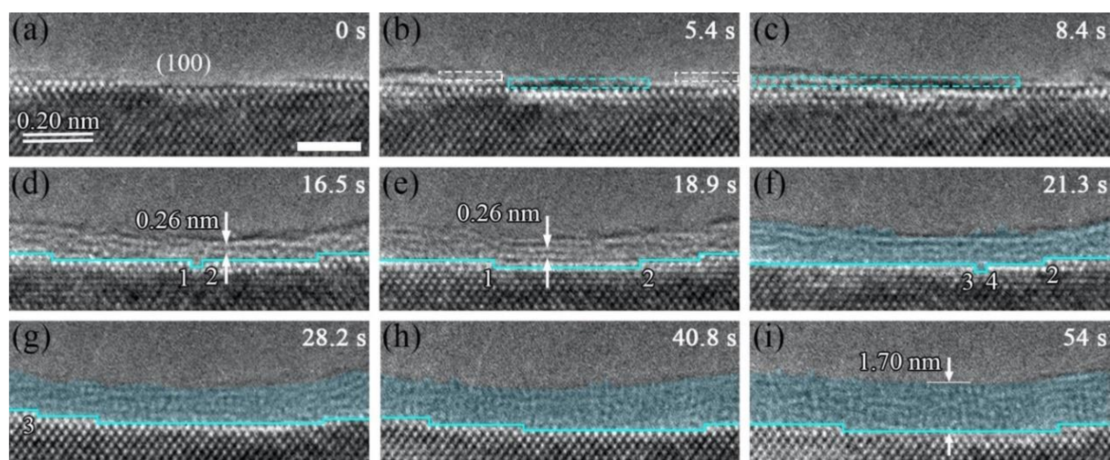

Figure S4. Passive oxide film formation on Al(100) (a-i) Time-sequence HRTEM images (Supplementary Movie 12) showing the layer-by-layer oxidation of the metal lattice into a paracrystalline oxide layer that subsequently transforms into an amorphous Al oxide layer upon the continued O_2 exposure at T=298 K in $pO_2 \approx 9.3\times10^{-3}$ Pa. The dashed white and cyan rectangles mark the weakened lattice contrast regions upon the O adsorption induced abstraction of Al atoms from the topmost surface region. The cyan lines mark the oxide/metal interface and lateral flow of interfacial ledges 1-4. Scale bar, 2 nm. The pseudo color is applied to the oxide layer to guide the eye.

SI-4. XPS measurements of the passive oxide film formation on Al(111)

For cross-validating the *in situ* TEM results, complementary X-ray photoelectron spectroscopy (XPS) was employed to obtain the global information on the passive oxide film formation on Al. XPS measurements were performed with in an ultrahigh vacuum system. The system is equipped with an XPS spectrometer (SPECS Phoibos 100 MCD analyzer), low-energy electron diffraction, and an Ar-ion sputtering gun. The chamber has a base pressure of 2.7×10^{-8} Pa. Al-Kα x-ray radiation was used for the XPS measurements. The Al(111) single crystal is a "top-hat" disk (1 mm thick and 8 mm in diameter), purchased from Princeton scientific Corp., cut to within 0.1° to the (111) crystallographic orientation and polished to a mirror finish. The crystal was cleaned by cycles of Ar^{+} bombardment at 298 K and annealing to 700 K. Oxygen gas (purity=99.9999%) was introduced to the system through a leak valve and the sample was oxidized at 298 K and $pO_2 \approx 1.3\times10^{-3}$ Pa. Fig. S5 shows the representative XPS spectra of the O 1s and Al 2p peaks obtained from the Al(111) after 5 min and 70 min of the O_2 exposure, respectively. The O 1s spectra with the binding energy (BE) of 532.3 eV correspond to the O in Al−O bonds due to the Al oxide formation. This corroborates with the Al 2p spectra that can be deconvoluted into the metallic (Al^{0}) component (BE = 72.8 eV) and the oxide component (Al^{3+}) (BE = 75.6 eV). The longer O_2 exposure time not only resulted in the increased intensity of both the O 1s and Al^{3+} 2p peaks but also the binding energy (BE) shift of the Al^{3+} 2p peak from BE=75.1 eV to 75.5 eV. Quantification of the XPS spectra shows that the area ratio of the O 1s and Al^{3+} 2p peaks increases from 7.3 (5 min of O_2 exposure) to 10.3 (70 min of O_2 exposure), indicating the enrichment of the O content in the oxide layer upon the continued O_2 exposure. This is further confirmed with the observed shift of the Al^{3+}(2p) peak toward the higher BE side, constant with previous XPS studies showing that a higher BE energy of the Al^{3+} 2p peak is induced by the increased O concentration in the aluminium oxide film.[1] Because the XPS has a much larger probed surface area (≈ 100 μm) than ETEM, prolonged periods of O_2 exposure were used in the XPS

experiment to fully oxidize the Al surface, thereby ensuring that the measured XPS signal is from the oxidized surface other than from any un-oxidized Al areas.

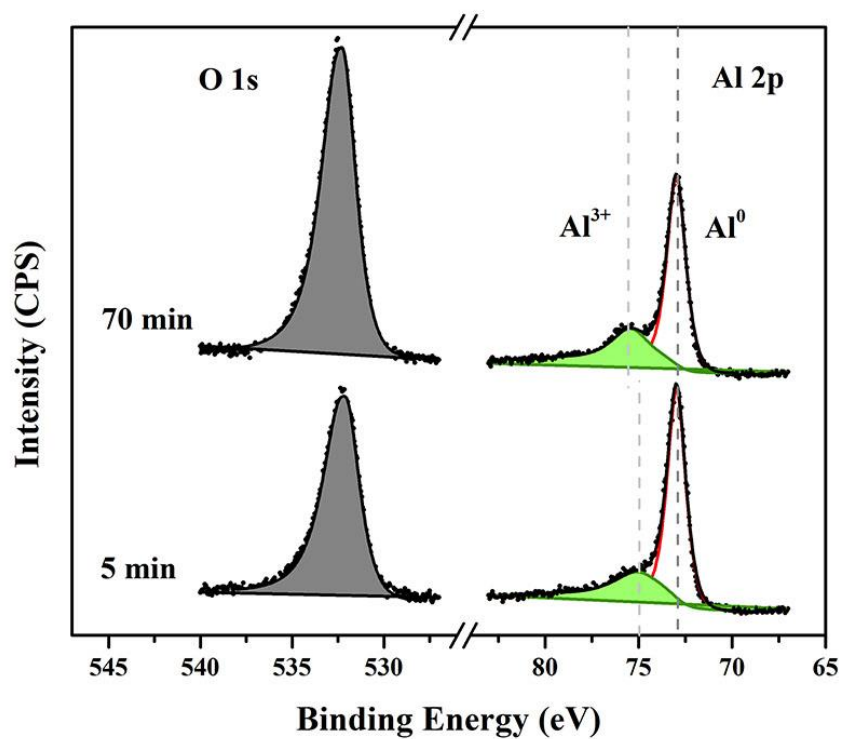

Figure S5. XPS measurement of the passive oxide film formation on Al(111). Photoemission spectra of the O 1s and Al 2p core-level regions obtained from the O_2 exposure at T=298 K and $pO_2 = 1.3\times10^{-3}$ Pa for 5 min and 70 min, respectively.

SI-5. Excluding electron beam irradiation effects on the TEM observations of the oxide film growth

One of the major concerns for *in situ* TEM experiments is the potential electron beam irradiation effects. Nguyen et al.[2] examined electron beam effects on Al oxidation and a safety zone, where the continuous electron beam observations do not induce noticeable differences to the oxide growth compared with the beam-blank oxidation experiments, has been identified to be an electron flux of < 12,000 e $Å^{-2}s^{-1}$. In our experiments, a highly condensed beam (dose rate ≥ 56000 e $Å^{-2}s^{-1}$) was used to sputter off the native oxide and obtain pristine surfaces while a significantly lower electron beam flux of ~ 6790 e $Å^{-2}s^{-1}$ was used to minimize the electron beam effect during the *in situ* TEM observations. Furthermore, potential TEM electron beam irradiation effects on the observed oxide film growth were carefully evaluated to ensure that an intrinsic behavior of the oxidation kinetics was studied. We performed "comparison experiments" at multiple surface locations by un-blanking and blanking the electron beam. This is also consistent with previous surface science experiments showing the negligible effect from the high-energy ion beam bombardment on the Al oxide film growth on Al(111).[3]

The Al oxide film growth is observed to reach a limiting thickness of ~ 2.5 nm after ~ 300 s of the O_2 exposure from our *in situ* TEM observations (Fig. S6). Figs. S6(a-e) present snapshot TEM images of Al oxidation with the continuous electron beam observation. Fig. S6(f) illustrates the average thickness of the oxide film as a function of oxygen exposure time, showing the oxide film growth to a limiting thickness over the extended period of the oxygen exposure. The growth curve measured from the *in situ* TEM imaging can be well fitted with the Cabrera-Mott model. The oxide film was then removed by condensing the e-beam to sputter off the oxidized region and thus restore the surface to the pristine state (Fig. S6(g)). The electron beam was then blanked off and the cleaned surface was thus oxidized "in the dark" under the same oxidation condition. During the oxidation, the electron beam was unblanked about every 60 s for

taking TEM images (Figs. S6(g-l)). As shown in Fig. S6(f)), the thickness of the oxide film measured with the electron beam off is in good agreement with that observed with the continuously imaged surface. Additionally, Fig. S7 displays the formation of paracrystal oxide layer followed by the transformation into the amorphous oxide "in the dark" with the progressive O incorporation. This is consistent well with the observed two-stage oxidation process under the continuous electron beam irradiation. These comparison experiments confirm that the e-beam irradiation effect on the oxide growth is negligible in our *in situ* TEM observations, which is also consistent with other *in situ* TEM work of Al oxidation.[2, 4]

It is also worth mentioning that previous work showed the enhanced Al oxidation by electron bombardment.[3a-3c] Such enhancement is attributed to the low energies (up to 100 eV) of incident electrons that can be effectively trapped by the oxide film formed on the bulk crystal, thereby resulting in the excitation of adsorbed gas molecules (O_2, H_2O, etc.) and the enhanced electrostatic field across the oxide film to promote the ion mobility. By contrast, our *in situ* TEM experiments use a much higher electron energy (300 KeV), for which the scattering cross-section (i.e., the effective area for collisions of the electrons with atoms in the TEM specimen) is much smaller. The mean-free path for 200-KeV electrons was measured using electron-energy loss spectroscopy (EELS) to be 134 nm and 140 nm for Al and Al_2O_3, respectively.[3d] In our *in situ* TEM experiments, the higher electron beam energy (300 KeV) gives rise to even greater mean-free paths that are much larger than the specimen thickness (~ 50 nm). Therefore, the chances for trapping incident electrons and inelastic scattering of the incident electrons are negligible. This is consistent with our "blanked-beam" and "unblanked-beam" experiments, showing the negligible differences in the oxide film thickness. Such a negligible effect from the continuous electron beam observations of Al oxidation was also confirmed by Nguyen et al.[2] While there are no electrons trapped by the TEM thin specimen because the incident electron beam transmits through the specimen, the knock-on damage by the high-energy electrons may result in the creation of atomic

defects in the oxide film. Previous surface science experiments showed the negligible effect from the high-energy ion beam bombardment induced defects on the Al oxide film growth on Al(111).[3a] This corroborates well with the results from our "beam-on" and "beam-off" experiments and the work by Nguyen et al.[2]

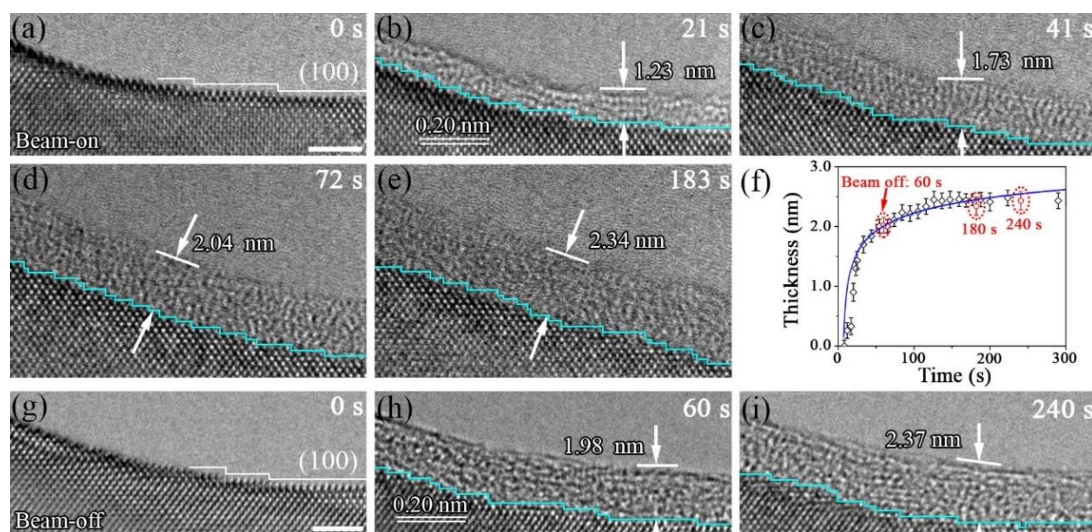

Figure S6. "Electron beam-on and beam-off" experiments showing the oxide film growth to the limiting thickness. (a-e) Time-sequence HRTEM images acquired with the continuous electron beam observation of the Al oxidation at T=298 K and $pO_2 \approx 8.6\times10^{-3}$ Pa. (f) The average thickness of the oxide film as a function of the oxygen exposure time. Superimposed on the experimental data points are theoretical fit to the inverse logarithmic growth law of the Cabrera-Mott theory. (g) The surface was recovered to the pristine state by sputtering off the oxide film with the condensed electron beam. (h, i) The electron beam was then blanked off and the cleaned surface was oxidized "in the dark" under the same oxidation condition. During the oxygen exposure, the e-beam was only unblanked for taking TEM images. The thickness of the oxide film measured with the blanked electron beam is given in (f), where the data points marked in red correspond to the thickness of the oxide film grown "in the dark", showing good agreement with that observed with continuously imaged surface. The cyan lines mark the oxide/metal interface. Scale bar, 2 nm.

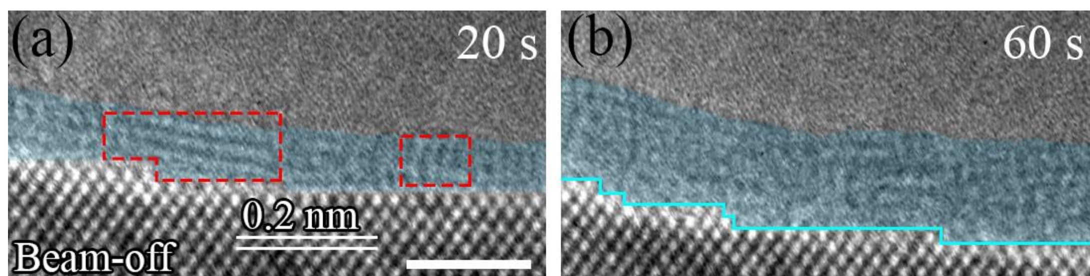

Figure S7. "Electron beam-off" experiments showing the two-stage oxide-film formation. (a) The formation of paracrystal oxide domains on a freshly clean Al surface after a time elapse of ~ 20 s, at T=298 K and $pO_2 \approx 7.3\times10^{-3}$ Pa, which is a neighboring area of the imaged regions. The dashed red rectangles mark the paracrystalline oxide regions. The surface was first cleaned by sputtering off the oxide film with the condensed electron beam. The electron beam was then blanked off and the cleaned surface was oxidized "in the dark". (b) The transformation of the paracrystal oxide into the amorphous oxide occurs "in the dark" upon the continued oxygen exposure, consistent with the real time TEM observations with the continuous electron beam irradiation. Scale bar, 2 nm. The pseudo color is applied to the oxide layer to guide the eye.

SI-6. Negligible effects from background gas molecules in the TEM column on the oxide formation

The E-TEM column has a base pressure of 3.6×10^{-5} Pa and the possible effect from background gas molecules (mostly hydrogen, water vapor, carbonyl) in the sample area on the TEM observed oxide film growth was examined. Fig. S8(a) is an HRTEM image of an as-prepared pristine Al surface. Fig. S8(b) corresponds to the surface after a time elapse of 120 s in vacuum, showing there was barely any oxide formation. In contrast, the surface shows obvious oxide growth within ~20 s upon the exposure to 7.3×10^{-3} Pa of O_2 gas flow, indicating the negligible effect from the background gas molecules on the observed oxide formation.

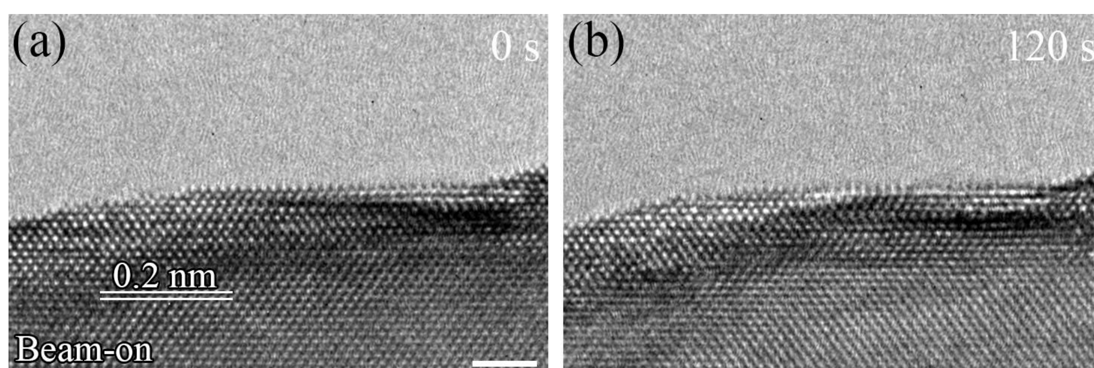

Figure S8. Negligible effect of the background gas molecules in the TEM column on the passivating oxide film growth. (a) The as-prepared Al surface by sputtering off the native oxides. (b) The same surface area after a time elapse of 120 s in vacuum, showing barely any oxide formation. Scale bar, 2 nm.

SI-7. ReaxFF MD simulations the oxidation of flat and stepped Al(111) surfaces

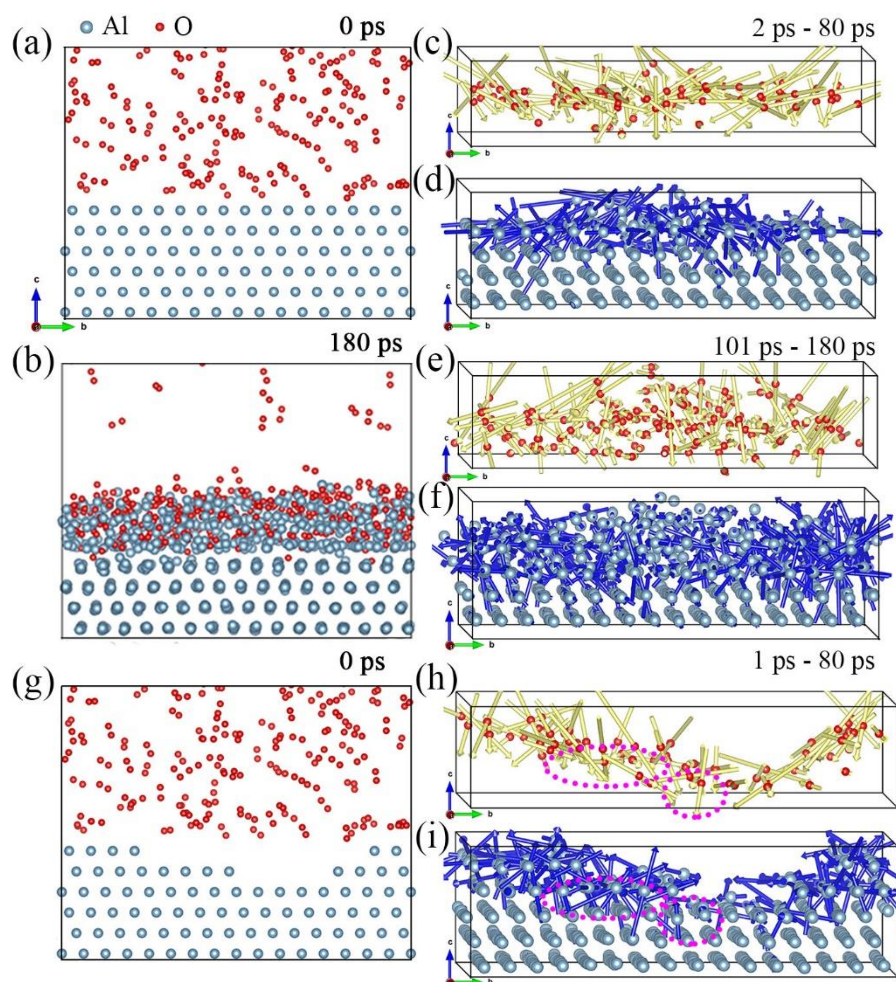

Figure S9. ReaxFF MD simulations of the oxidation of flat and stepped Al(111) surfaces at T=298 K and pO_2 = 0.2 g/cm^3**.** (a, b) Snapshots of MD simulations of the oxidation of a flat Al(111) surface at 0 ps and 180 ps of O_2 exposure (Supplementary Movies 13, 14). (c, d) Displacement vectors of O and Al atoms between 2 ps and 80 ps of O_2 exposure. (e, f) Displacement vectors of O and Al atoms between 101 ps and 180 ps of O_2 exposure. (g-i) MD simulations of the oxidation of a stepped Al(111) surface and displacement vectors of O and Al atoms between 1 ps and 80 ps of O_2 exposure (Supplementary Movie 15). The dashed magenta circles in (h, i) mark the stepped region, showing locally promoted interlayer displacement of O and Al atoms. The blue and red balls represent Al and O atoms, and the golden and blue arrows correspond to the atomic displacement vectors of O and Al atoms, respectively.

SI-8. DFT modeling of the oxygen adsorption on stepped Al(100) and (111) surfaces

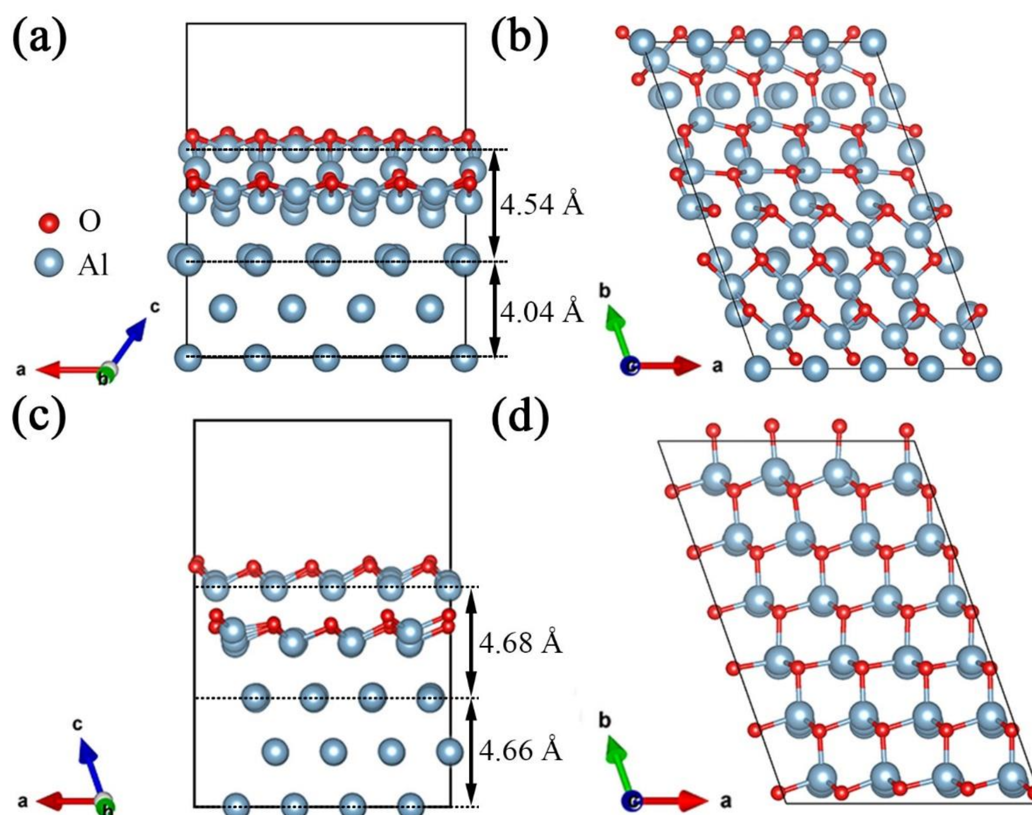

Figure S10. DFT-relaxed structure of the stepped Al(100) and (111) surfaces covered with a monolayer of pre-adsorbed O. (a, b) Side and projection views of the oxygenated Al(100) surface. (c, d) Side and projection views of the oxygenated Al(111) surface. The resultant lattice distortion of O and Al atoms in the surface layer bears a reasonable resemblance to a thin layer of amorphous Al oxide with the resulting oxide/metal interfaces.

Caption for supplemental movies:

Supplementary Movie 1 (the movie from which Figure. 1 is extracted): *In situ* TEM movie showing the oxidation of Al(111) at T=298 K and $pO_2 \approx 7.3\times10^{-3}$ Pa.

Supplementary Movie 2 (the movie from which Figure. 2 is extracted): *In situ* TEM movie showing the oxidation of Al(100) at T=298 K and $pO_2 \approx 7.3\times10^{-3}$ Pa.

Supplementary Movie 3 (the movie from which Figures. 3(a-d) are extracted): *In situ* TEM movie showing the oxidation of an Al(111) surface consisting of terraces and well-separated monatomic steps at T=298 K and $pO_2 \approx 7.3\times10^{-3}$ Pa.

Supplementary Movie 4 (the movie from which Figures. 3(e-h) are extracted): *In situ* TEM movie showing the oxidation of an Al surface consisting of highly stepped regions and relatively wide terraces at T=298 K and $pO_2 \approx 7.3\times10^{-3}$ Pa.

Supplementary Movie 5 (the movie from which Figures. 3(i-l) are extracted): *In situ* TEM movie showing the oxidation of a highly stepped Al surface at T=298 K and $pO_2 \approx 7.3\times10^{-3}$ Pa.

Supplementary Movies 6 and 7 (the movies from which Figures. 5(a-f) are extracted): ReaxFF MD simulations of the oxidation of Al(100) at T=298 K and pO_2 = 0.2 g/cm^3.

Supplementary Movie 8 (the movie from which Figures. 5(g-i) are extracted): ReaxFF MD simulations of the oxidation of a stepped Al(100) surface at T=298 K and pO_2 = 0.2 g/cm^3.

Supplementary Movie 9 (the movie from which Figure. S3 is extracted): *In situ* TEM movie showing the oxidation of an Al(111) surface at T=298 K and $pO_2 \approx 9.3\times10^{-3}$ Pa.

Supplementary Movie 10 (the movie from which Figure. S4 is extracted): *In situ* TEM movie showing the oxidation of an Al(100) surface at T=298 K and $pO_2 \approx 9.3\times10^{-3}$ Pa.

Supplementary Movies 11 and 12 (the movies from which Figures. S9(a-f) are extracted): ReaxFF MD simulations of the oxidation of Al(111) at T=298 K and pO_2 = 0.2 g/cm^3.

Supplementary Movie 13 (the movie from which Figures. S9(g-i) are extracted): ReaxFF MD simulations of the oxidation of a stepped Al(111) surface at T=298 K and pO_2 = 0.2 g/cm^3.

Supplementary References

[1] a) U. Bardi, A. Atrei, G. Rovida, *Surf. Sci.* **1992**, 268, 87; b) J. Zähr, S. Oswald, M. Türpe, H. J. Ullrich, U. Füssel, *Vacuum* **2012**, 86, 1216.

[2] L. Nguyen, T. Hashimoto, D. N. Zakharov. E. A. Stach, A. P. Rooney, B. Berkels, G. E. Thompson, S. J. Haigh, T. L. Burnett, *ACS Appl. Mater. Interfaces.* **2018**, 10, 2230.

[3] a) I. Popova, V. Zhukov, J. T. Yates, *Phys. Rev. Lett.* **2002**, 89, 2; b) H. D. Ebinger, J. T Yates, *Phys. Rev. B* **1998**, 57, 1976; c) I. Popova, V. Zhukov, J. T. Yates Jr, J. G. Chen, *J. Appl. Phys.* **1999**, 86, 7156; d) K. Iakoubovskii, K. Mitsuishi, Y. Nakayama, K. Furuya, *Phys. Rev. B* **2008**, 77, 104102.

[4] Y. Yang, A. Kushima, W. Z. Han, H. L. Xin, J. Li, *Nano Lett.* **2018**, 18, 2492.